




New Vacuum Solar Telescope Achieves Narrowband Infrared Solar Imaging Observation at He I 10830 Å

Wei-Jie Meng^{1,2,3} , Fang-Yu Xu^{1,2}, and Zhen-Yu Jin^{1,2}

¹ Yunnan Observatories, Chinese Academy of Sciences, Kunming 650011, China; xu_fangyu@ynao.ac.cn

² Yunnan Key Laboratory of Solar Physics and Space Science, Kunming 650216, China

³ University of Chinese Academy of Sciences, Beijing 100049, China

Received 2024 January 31; revised 2024 March 21; accepted 2024 March 25; published 2024 May 2

Abstract

The near-infrared imaging channel constitutes a crucial component of the multichannel high-resolution imaging system of the New Vacuum Solar Telescope (NVST). We have successfully achieved high-resolution, narrowband imaging of the chromosphere using He I 10830 Å triplet within this channel, which significantly enhances the imaging observation capabilities of NVST. This paper provides a concise overview of the optical system associated with the near-infrared imaging channel, detailing data processing procedures and presenting several observed images. Leveraging a high-resolution image reconstruction algorithm, we were able to generate a narrowband image near the diffraction limit at 10830 Å with a temporal resolution of less than 10 s.

Key words: instrumentation: detectors – instrumentation: high angular resolution – Sun: chromosphere – Sun: infrared

1. Introduction

The New Vacuum Solar Telescope (NVST) serves as a pivotal ground-based telescope within China's solar research community, offering unparalleled observational capabilities. Its principal objective is to attain high-resolution imaging and spectroscopic observations in the optical and infrared bands, ranging from 0.3 to 2.5 μm , inclusive of measurements of the solar magnetic field (Liu et al. 2014). Recently, in collaboration with the Kunming Institute of Physics, the astronomical technology laboratory at Yunnan Observatories has embarked on the development of high-performance near-infrared cameras. Since 2022 August, a near-infrared camera has been operationally capable of initially satisfying the requirements for high-resolution narrowband imaging, and a series of observation imaging experiments have been conducted.

The detailed examination of the fine structure within both the photosphere and chromosphere is a primary scientific objective for NVST, particularly its multi-channel high-resolution imaging system (Xu et al. 2014). The H α (6563 Å) and TiO (7058 Å) channels, which simultaneously observe the chromosphere and photosphere, have significantly contributed to the international solar community. Given the requirements of the multi-channel high-resolution imaging system and the near-infrared solar spectrum accessible at ground-based solar telescopes, we chose He I 10830 Å as a breakthrough line to initially achieve high-resolution observation of NVST in the near-infrared band. He I 10830 Å is essentially a triplet line mainly formed in the upper chromosphere, proximate to the

base of the corona (Avrett et al. 1994). Among the spectra accessible at ground level, observations of the solar atmosphere using He I 10830 Å are distinctive, which exhibit characteristics of coronal features such as coronal holes, bright points, and hot footpoints of large magnetic structures associated with matter ejection (Harvey & Livingston 1994). The morphology of the chromosphere with the photosphere and corona under the H α spectral line, commonly used by ground-based solar observatories, differs significantly, making it challenging to elucidate the physical connection between the photosphere and corona. In contrast, the He I 10830 Å line exhibits a significantly thinner optical thickness compared to other chromospheric lines such as H α and Ca II lines. This characteristic allows for the photosphere to shine in as a distinct background. Consequently, specific photospheric features can be discerned from imaging, thereby facilitating the tracking of solar activity from the photosphere to the low corona (Ji et al. 2012). Therefore, the imaging observation of He I 10830 Å conducted on NVST can serve as a substantial data supplement for the multi-channel high-resolution imaging system. The He I triplet line is also a crucial tool for diagnosing chromospheric vector magnetic fields (Trujillo Bueno et al. 2002). We aim to enhance NVST's capability to measure solar vector magnetic fields based on this imaging work, and NVST will be tasked with additional scientific and technical responsibilities.

Traditionally, two primary techniques have been utilized to obtain 2D imaging spectra (Chae et al. 2013). The first approach employs tunable narrowband filters to collect

monochromatic images of the solar atmosphere across different wavelengths, a method referred to as filtergraph system. Conversely, the second technique involves capturing a sequence of spectra as the spectrometer's slit scans the designated region, a process known as the grating spectrograph system. GST\NIRIS (Cao et al. 2012) employs the former method, utilizing a double Fabry–Pérot Interferometers with an $85''$ circular field of view to image on a Teledyne developed 2048×2048 array HgCdTe camera. Polarization observation is facilitated by rotating waveplates and two Wollaston prisms, primarily using the Fe I $1.565 \mu\text{m}$ doublet line and He I $1.083 \mu\text{m}$ triplet line. With the aid of broadband auxiliary channel, high-resolution image reconstruction is accomplished through the speckle masking method. GRECOR\GRIS (Regalado Olivares et al. 2022) and DKIST\DLNIRSP (Jaeggli et al. 2022) adopt the latter method and can further use integral field units for solar observation and of course polarization spectroscopy in the near-infrared. The near-infrared imaging channel of NVST in this paper utilizes the former method.

In the subsequent section, we provide a succinct introduction to the near-infrared imaging channel of NVST. The methodology employed for acquiring and processing near-infrared data is delineated in Section 3. Additionally, select He I 10830 Å imaging data obtained by our team are showcased.

2. The Near-infrared Imaging Channel

The near-infrared imaging channel is part of the multi-channel high-resolution imaging system of NVST, which includes the H α and TiO channels and is situated on a rotating optical platform with a diameter of 6 m. The H α and TiO channels have been operational for approximately 10 yr, whereas the near-infrared imaging channel has recently been commissioned. This comprehensive system can function independently or integrate with the adaptive optics (AO) system to operate as an AO multi-channel imaging system. While all channels can operate concurrently, the simultaneous observation of the NIR channel with the H α and TiO channels has not yet been accomplished. However, we anticipate that this capability will be achieved in our forthcoming retrofit program. The near-infrared channel employs a near-infrared Lyot filter with a Full Width at Half Maximum (FWHM) of 0.5 Å , developed by the Nanjing Institute of Astronomical Optics and Technology. Under optimal seeing conditions, without AO, the spatial resolution of the chromosphere image reconstructed by the statistical high-resolution algorithm for the 10830 Å band can nearly reach $0''.3$, with the time interval for reconstructing images approximately being 10 s. Table 1 provides some key parameters of the current NVST imaging system (Liu et al. 2014).

Regrettably, due to the considerably narrow spectral line of the He I 10830 Å triplet, it is a significant challenge to achieve

Table 1
Parameters of the NVST Imaging System

Channel	H α	TiO	10830
Filter	Lyot Filter	Interference Filter	Lyot Filter
Wavelength (Å)	6562.8 ± 4	7058	10830
Bandpass (Å)	0.25	10	0.5
Focal length (m)	22.5	35(26)	20.58
FPS	10	10	55
FOV	$180'' \times 180''$	$180'' \times 180''$	$96'' \times 76''$

an accurate spectral profile with this filter. According to the published spectra data,⁴ the FWHM of He I 10830 Å triplet in the quiet region has been calculated to be 0.48 Å , while the FWHM of the Lyot filter is about 0.5 Å , as shown in Figure 1. However, both the acquisition of velocity fields related to solar activity dynamics processes and the realization of polarization observations necessitate the procurement of high-precision spectral line profile data. This necessitates the utilization of a filter characterized by a narrower passband and an enhanced transmittance and redesigning of corresponding optical paths.

2.1. NIR Camera

At present, the sole near-infrared camera available for NVST is a 640×512 InGaAs CMOS camera, developed collaboratively by Yunnan Observatories and Kunming Institute of Physics in 2022. The camera is characterized by an exceptional maximum frame rate of 300 frame/s, achieved through the utilization of eight independent readout channels. Furthermore, it offers three gain modes to accommodate varying operational scenarios. On the multi-channel high-resolution imaging platform of NVST, the preferred choice is the medium gain mode. The exposure time can be modulated within a range of 12–20 ms, contingent on weather conditions. Besides, for those requiring superior time resolution, the high gain mode is an option. Detailed performance parameters of this camera are presented in Table 2.

To mitigate the interference fringes observed in narrowband imaging, a wedged glass with an angle of $1^\circ 37'$ was employed to seal the camera. Additionally, the camera's spectral response range has been measured to be between 1000 and 1580 nm, demonstrating a quantum efficiency exceeding 50% within this wavelength range.

While the camera initially satisfies the observational requirements of NVST in the near-infrared band, several issues persist. First, the array size is limited: the objective of a multi-channel high-resolution imaging system is to achieve imaging observation near the diffraction limit. The Rayleigh diffraction limit of NVST at 10830 Å is about $0''.278$, and the maximum spatial sampling resolution, as defined by the Nyquist sampling

⁴ https://bass2000.obspm.fr/solar_spect.php

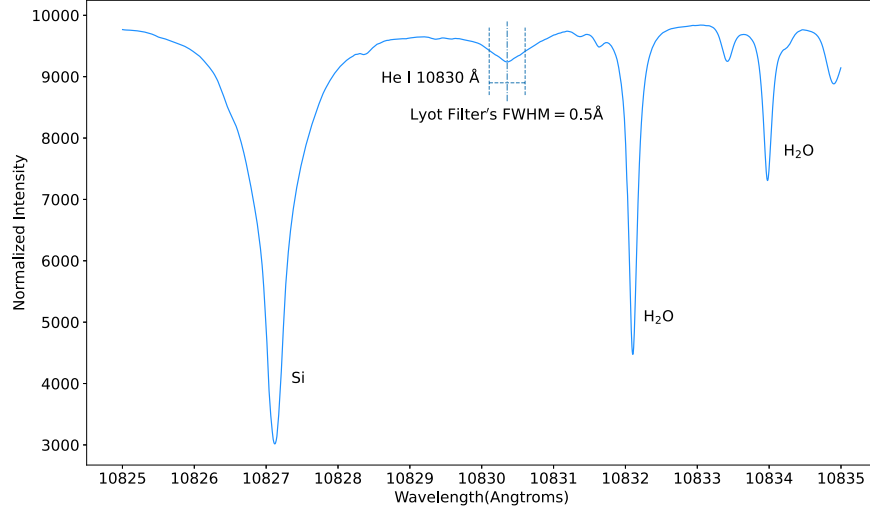


Figure 1. Solar spectrum of the quiet region near He I 10830 Å. The distance between the two dashed lines is denoted as 0.5 Å, which signifies the FWHM of the Lyot filter passband.

Table 2
Parameters of the NIR Camera

Parameter	Value
Detector material	InGaAs
FPA format	640 × 512
Pixel size	15 μm × 15 μm
Operating wavelengths	1.0 ~ 1.58 μm
Quantum efficiency	≥70% @ 1.083 μm
Charge to digital conversion factor	0.28 e ⁻ /ADU @ high gain
Readout noise	28.65 e ⁻
Well capacity	2.05 × 10 ⁴ e ⁻
Dark current	3.64 × 10 ³ e ⁻ /(s pixel)
Photoresponse nonlinearity	<0.1%
Blind element rate	<0.6%
Cooling system	Stirling Cooling (77 K)
Frame rate	Up to 300FPS
Grayscale	16 bit

law, is $0''.139 \text{ pixel}^{-1}$. However, the current actual spatial sampling resolution stands at $0''.15 \text{ pixel}^{-1}$, indicating under-sampling. Consequently, the field of view of the focal plane array measures $96'' \times 76''$. This limited field of view is insufficient for observing an active region with a large scale. Second, the dark current noise is substantial: The camera's dark current level is $3.64 \times 10^3 e^-/(\text{s pixel})$. When the exposure time is set to 15 ms at medium gain, the dark current noise approximates $7.4 e^-/\text{pixel}$. Third, there exists column fixed mode noise: while the primary column fringe noise can be rectified using flat-field correction, residual fringes persist in areas with low gray values. Although many classical image processing methods can eliminate these residual column

fringes, they invariably impact the intensity distribution of specific image areas to varying extents.

3. Data Processing

During the observation process, a series of dark fields are typically captured, along with flat fields taken in both morning and afternoon. This is due to the need for the alt-az telescope to be adjusted after reaching its limit throughout the day, which can result in alterations to the flat field. The exposure time for the data is kept as consistent as possible with that of the dark field and flat field, although it should also be adjusted based on the specific conditions and requirements of the observation. The primary processing procedure for 10830 Å imaging data encompasses several steps: flat and dark field processing, initial alignment of data, solar image reconstruction based on non-rigid alignment, and alignment of the reconstructed data.

3.1. Data Preprocessing

The pixel output voltage signal of a CMOS camera equipped with a CDS (Correlated Double Sampling) function, following the application of a programmable analog gain amplifier, can be represented by the given formula (1) (Li et al. 2021)

$$V_{\text{pixel}} = G \cdot \frac{(I_p + I_d) \cdot T}{C} + V_{\text{offset}}. \quad (1)$$

In this context, G denotes the amplification gain, V_{offset} signifies the bias voltage of the amplifier, which is utilized to establish the static working point of the amplification circuit. This ensures that the circuit operates within the linear amplification region. Additionally, I_p and I_d represent the photocurrent and dark current respectively. T represents the integration time, while C symbolizes capacitance.

The formula clearly illustrates that the bias noise $G \frac{I_d T}{C}$ and V_{offset} , introduced by dark current and the amplifier respectively, can be mitigated through frame subtraction, a process known as dark field processing. The nonuniformity of response, which is induced by the amplification circuit G and other factors, can be curtailed by dividing by the detector's response to a uniform field, a method referred to as flat field processing. This is also the rationale behind the suppression of the aforementioned fringe noise through flat-and-dark processing. However, it is not possible to eliminate column fringes due to potential instability in G and V_{offset} .

The preprocessing procedure for the 10830 Å data set can be succinctly articulated using the following formula (2)

$$O = \frac{I - K}{F - K}. \quad (2)$$

In this context, I denotes the raw target data obtained, while K and F symbolize the average dark field and average flat field respectively. Lastly, O represents the processed target data.

The dark-field K typically encompasses noise introduced by bias voltage, dark current, and stray light received by the focal plane array (FPA). It is important to note that the dark field can vary based on observations, such as changes in bias voltage and dark current due to temperature fluctuations, and stray light influenced by mechanical movements of the telescope and optical platform. Consequently, it is advisable to gather background and target data under conditions that closely resemble these environmental variations to mitigate the impact of inherent background shifts. In prior observation experiments, we collected several sets of dark field data with different exposure times at an interval time of 2 hr. The average dark field K derived from separate superposition averaging of two groups with identical exposure time are largely comparable; however, a discernible difference remains, indicating minor alterations in the dark field. This discrepancy primarily accounts for why the column fringe noise cannot be eliminated but merely suppressed.

Flat-field F is primarily employed to rectify nonuniformities in the detector's response, which can arise from a variety of factors such as variations in FPA pixel quantum efficiencies, discrepancies in analog amplifiers, the presence of halos or dirt on windows, and interference fringes induced by the windows. In contrast to the conventional method of acquiring flat field in night astronomy, which typically employs dawn and dusk light as a uniform source, two distinct methods can be utilized for obtaining solar flat-field. The first method involves defocusing the telescope to blur the solar surface structure, thereby achieving a uniform effect, which is then processed through averaging multiple frames. The second method entails randomly shaking the telescope's field of view, followed by processing through averaging multiple images. Defocusing the telescope significantly alters the optical structure of the system, potentially leading to the dispersion of speckle-like images or

modification of the pattern of fringes on the optical mirror, both of which hinder the objective of flat-field processing. In practical applications, random shaking of the telescope is generally employed to obtain flat-field data that capture the nonuniformity of the entire observation system. During actual observations, approximately 10,000 frames of flat field data are collected before the commencement of morning observations and after the conclusion of afternoon observations, with both sets having an exposure time identical to that of target data. The average flat-field F for morning and afternoon is obtained through multiframe superposition averaging.

Upon acquiring the average flat-field F and average dark-field K , raw target data can be flat-dark fielding. Given that the adaptive optics system is not operational during observation, it is imperative to conduct a preliminary alignment of the flat-and-dark-fielded target data. This alignment leverages the cross-correlation subpixel-level translation algorithm to mitigate image jitter, which may arise from telescope tracking inaccuracies or wind loads. Additionally, it reduces image shifts resulting from wave front tilting due to proximate ground turbulence. Once this preliminary alignment is achieved, high-resolution image reconstruction can be executed using the Non-rigid Alignment based Solar Image Reconstruction (NASIR) algorithm.

3.2. High-resolution Image Reconstruction

To achieve near-diffraction-limited imaging of ground-based telescopes, in addition to the adaptive optics technology that corrects wave front distortion caused by atmospheric turbulence in real-time, post-processing high-resolution image reconstruction techniques are widely used on ground-based telescopes. NVST is equipped with an adaptive optics system, but unfortunately, the AO system was not enabled recently, so we rely more on post-hoc high-resolution image reconstruction techniques to obtain near-diffraction-limited imaging. Presently, two primary categories of high-resolution image reconstruction techniques exist for solar observations: the first being speckle imaging, which relies on the statistical analysis of various orders within the speckle images; and the second being multiframe blind deconvolution and phase difference methods for the Sun, which utilize the deconvolved instantaneous point-spread function. For narrowband imaging of He I 10830 Å, we employ the Non-rigid Alignment based Solar Image Reconstruction algorithm (Liu et al. 2022) developed by researcher Hui Liu at Yunnan Observatories. This method synergizes the swiftness of the Shift-Add technique with the precision of the speckle masking method. It establishes a computational model that links geometric distortion with intensity distribution, reconstructing the target image's phase at different frequencies. The modulus of the target image is then reconstructed using speckle interferometry. In scenarios with poor seeing, NASIR demonstrates superior robustness and

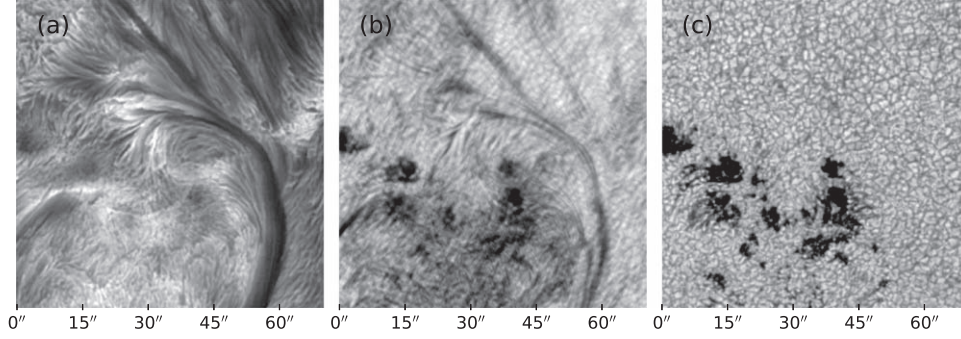


Figure 2. Filtergrams observed with NVST, showing different imaging characteristics in $H\alpha$, He I 10830 Å and TiO bands within the same FOV from (a) to (c).

reduced reconstruction time compared to the speckle masking method. Typically, we employ short exposure images (approximately 12 ms) of 500 frames to reconstruct a high-resolution image. The time resolution of this reconstructed image is dictated by the observation duration of a specific set of data sequences. The scanning and readout speed of the near-infrared camera ensures that the time resolution remains within 10 s. Leveraging the existing data processing system of NVST, we have achieved high-speed parallel processing for 10830 Å imaging data. Given the current volume of data is not substantial, it necessitates fewer resources to accomplish the quasi-real-time reconstruction of 10830 Å imaging data. We present a comparative analysis of the imaging characteristics of AR 13 323 in $H\alpha$, He I 10830 Å and TiO bands within the same Field of View (FOV) as depicted in Figure 2.

4. Observations in the NIR Channel

On 2023 June 5, NVST conducted a regular observation of AR 13 323. We extracted data from the UT 01:43–02:46 time frame, which included 10830 Å narrowband imaging data and TiO 7058 Å broadband imaging data. We also used a subset of the spatial observations of Solar Dynamics Observatory/Atmospheric Imaging Assembly (SDO/AIA: Pesnell et al. 2012; Lemen et al. 2012) at the same time. To align the NVST 10830 Å images with SDO/AIA images, we performed co-alignments using NVST TiO 7058 Å broadband images and Helioseismic and Magnetic Imager (HMI: Scherrer et al. 2012) continuum images as intermediaries. The specific registration method and details can refer to the work of Ji et al. (2019). In Figure 3, we present four image sets with the same FOV of $70'' \times 70''$ for a segment of AR 13,323 observed in the 10830 Å of NVST and the 1600, 304, and 131 Å of SDO/AIA, respectively. The figure roughly depicts the eruptive process near the filament footpoint, and to some extent shows the co-alignment of different band images.

Specifically, we follow Hong et al. (2017) and Hashim et al. (2024) to analyze the EUV moss region (FOV: $12'' \times 12''$, red box in Figure 3) preliminarily but only at 10830, 131, and

304 Å. Figure 4(a) shows an example of a 10830 Å filtergram taken at UT 02:34:54, with the FOV corresponding to the red box region in the first panel of Figure 3. Following the work of Hong et al. (2017) and Hashim et al. (2024), we divide the area into two regions: enhanced absorption patches (EAPs) and low absorption patches (LAPs). To contour the EAPs at a specific point in time, they are characterized as darker regions that do not surpass 90% of the average intensity within that area. This 90% is an empirical value, as Hong et al. (2017) identified it to correspond to the mean intensity along thin dark loops bridging two plage regions of the active region. For a comparative analysis, Figure 4(b) presents the TiO 7058 Å broadband photosphere image from an identical FOV. The photospheric features depicted in the 10830 Å filtergram bear a resemblance to those observed in the TiO image. However, in contrast to standard photosphere images, the 10830 Å image displays an increased number of absorption features, predominantly distributed along the intergranular lane areas. To further elucidate this, we overlay the contours (represented in black) from Figure 4(a) onto the TiO image, highlighting the white contoured area for clarity.

To illustrate the relationship between EUV emissions (only at 131 and 304 Å) and intensity of 10830 Å within the study region, we overlaid the EUV images with the contours of the EAPs from nearly simultaneous 10830 Å filtergrams, as shown in Figures 4(c) and (d). It can be found that the majority of the brighter regions in both the 131 and 304 Å emissions lie within the contours of the EAPs at 10830 Å. Figures 5(a) and (b) give the time profiles of EUV emissions at 131 and 304 Å on EAPs (red solid line) and LAPs (black dashed line), respectively. The emissions at 131 and 304 Å on EAPs are generally stronger than those on LAPs. This is consistent with the results shown in Figures 4(c) and (d). Figure 5(c) gives the time profiles of 10830 Å intensity on EAPs (red solid line) and LAPs (black dashed line), respectively. The intensity at 10830 Å on EAPs is generally weaker than that on LAPs, which is in accord with the results shown in Figure 4(a). Figure 5(d) shows the weak

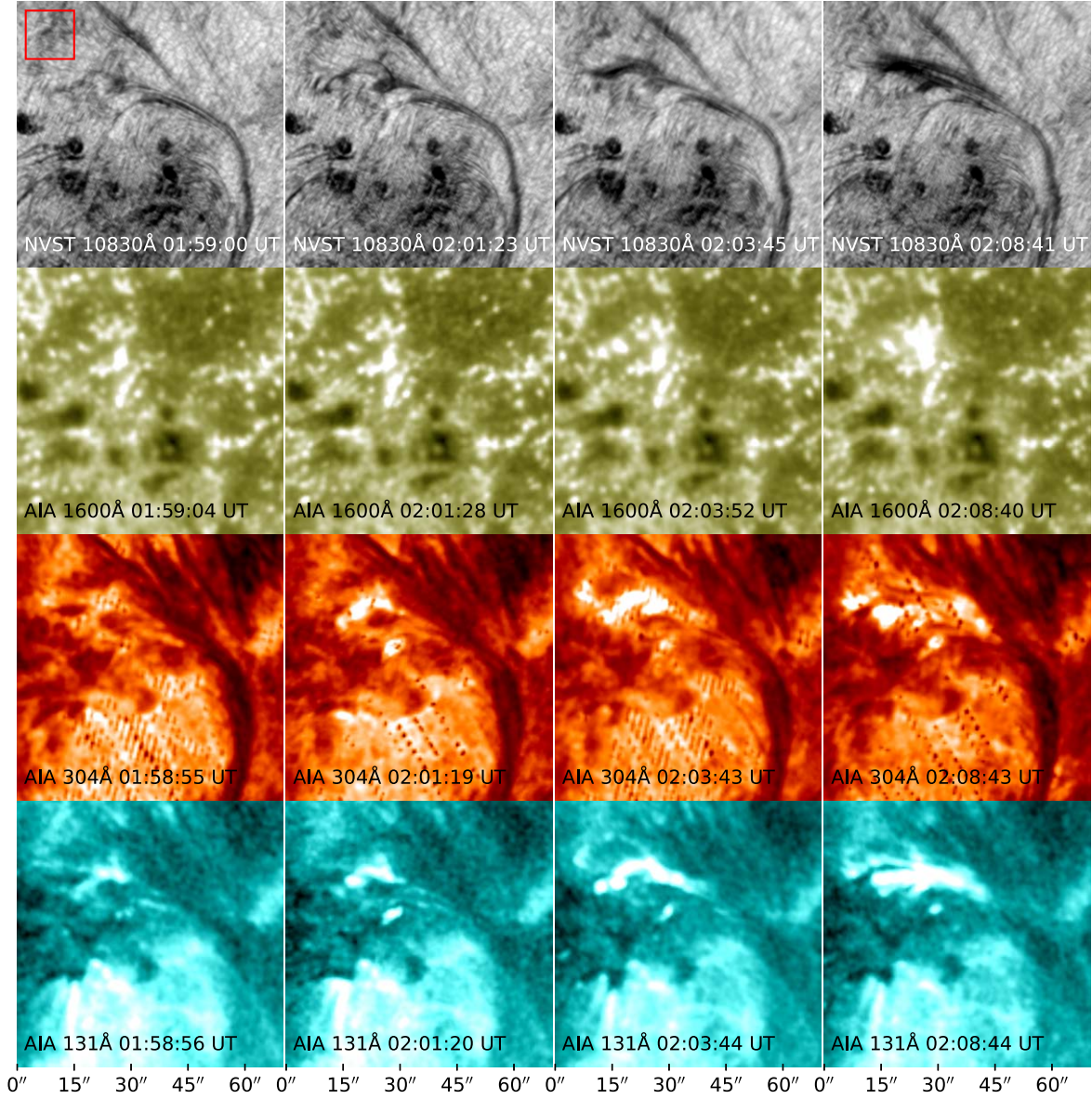


Figure 3. Snapshots of four sets of part of AR 13 323 observed in NVST 10830 Å, AIA 1600 Å, 304 Å, and 131 Å, showing the eruptive process near the footpoint region of the filament.

negative correlation between the emissions of EUV at 131 Å and intensity at 10830 Å on EAPs.

In conclusion, we examined 10830, 131, and 304 Å in our preliminary data analysis of the EUV moss region. Our findings indicate that the emissions of EUV at 131 and 304 Å on EAPs surpass those on LAPs, while the intensity of 10830 Å on EAPs is comparatively weaker. Furthermore, a negative correlation is observed between the emissions of 131 Å and the intensity of 10830 Å on EAPs. These preliminary results agree with the findings of Hong et al. (2017) and Hashim et al. (2024).

5. Summary

Despite the current capabilities of the near-infrared imaging channel in the multi-channel high-resolution imaging system of NVST, which can execute high-resolution narrowband imaging at the line center of the He I 10830 Å triplet using a Lyot filter with a bandwidth of 0.5 Å and the 640×512 near-infrared camera, several issues persist in the imaging process. The first issue is that the He I triplet is an extremely narrow spectral line, which makes it a challenge to the acquisition of high-precision spectral profile data with the running Lyot filter. Soon, we will

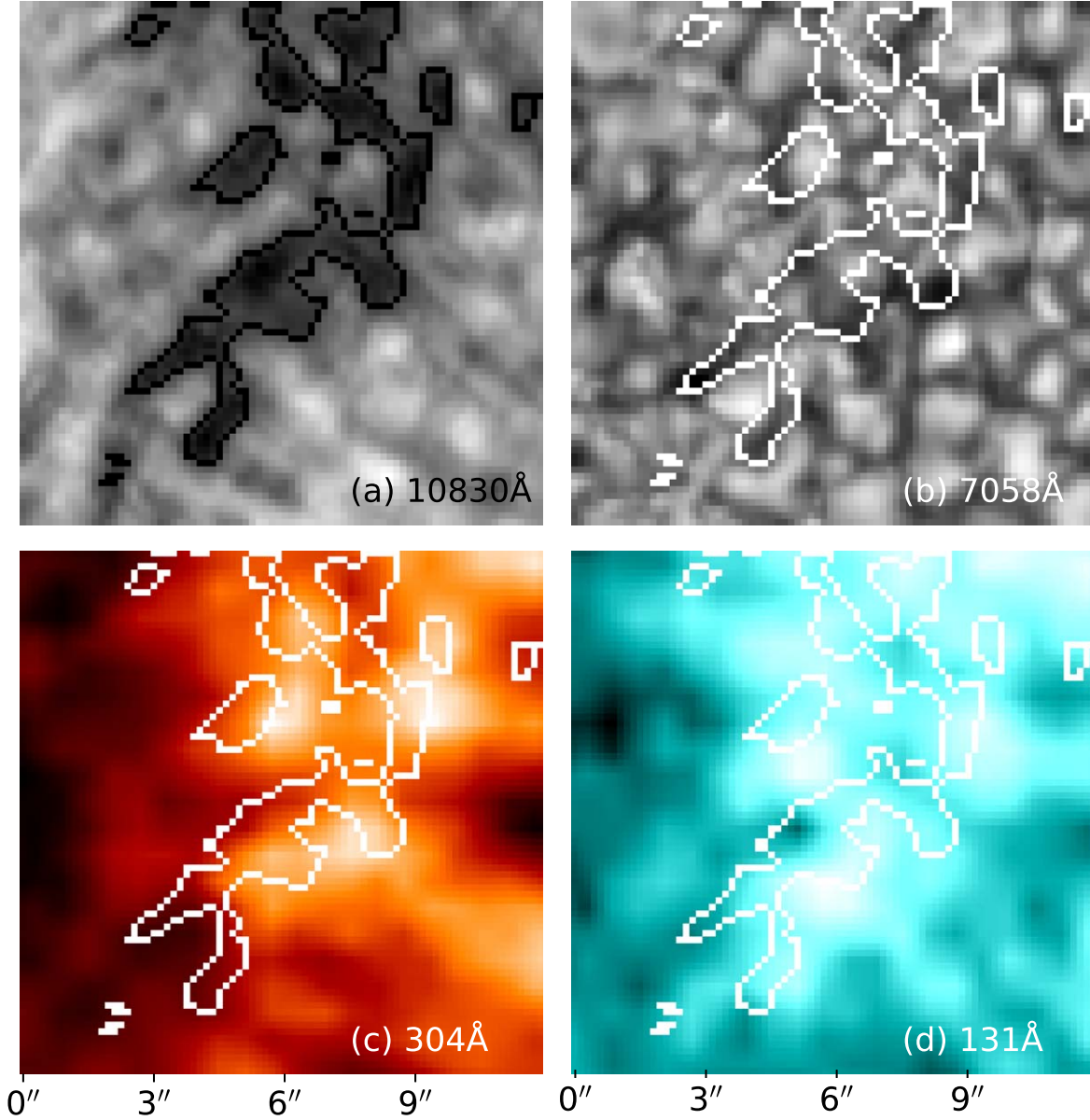


Figure 4. Panel (a): The He I 10830 Å narrowband filtergram overlaid with contours (in black) representing 90% of the mean intensity of the region. Panels (b)–(d) are snapshots of TiO 7058 Å and SDO/AIA images at 304 and 131 Å, respectively, overlaid with contours (in white) from panel (a). These images were taken at around 02:34:54 UT.

incorporate a Fabry–Pérot Interferometer with a more constricted passband and enhanced transmittance compared to the Lyot filter, necessitating a reconfiguration of the optical path. Additionally, issues such as the insufficient size of the array for the near-infrared camera and high dark current level are being addressed by the next generation of 1280×1024 camera. As of 2023 December, the latest prototype demonstrates a dark current level of $128e^-/(s \text{ pixel})$ and readout noise of $18.8e^-$ and its quantum efficiency is not inferior to the currently operational NIR detector.

Observational data of He I 10830 Å, inclusive of images and movies, are readily accessible at the Fuxian Lake Solar Observatory.⁵ The initiation of regular observation in the near-infrared channel enhances the multi-band high-resolution solar observation capability of NVST. The scientific data procured from this enhancement will serve as a significant supplement to the observational data gathered by global solar telescopes. Notably, the benefits of infrared bands in solar

⁵ <https://fso.ynao.ac.cn/>

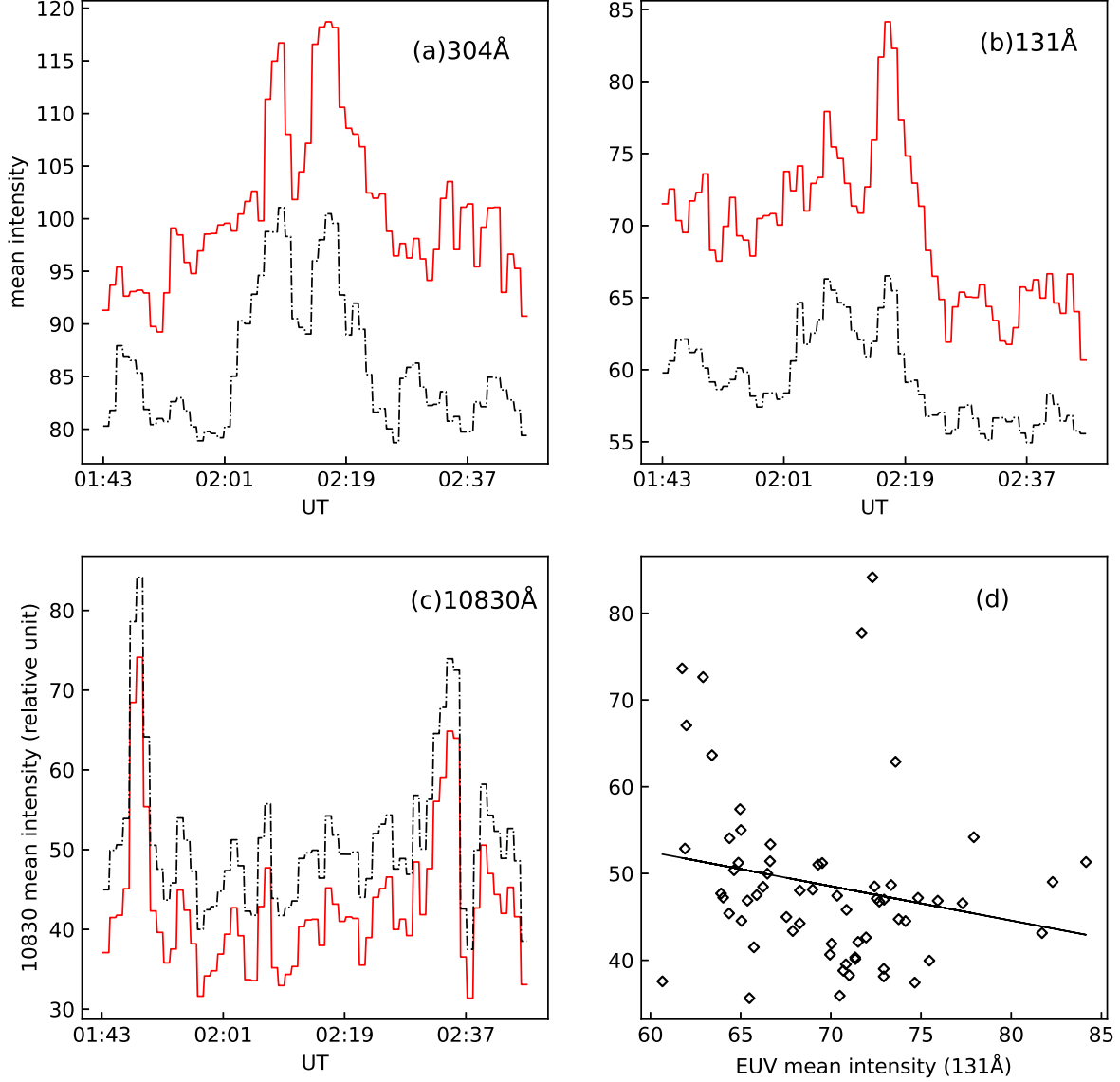


Figure 5. Panels (a)–(b): Time profiles of average EUV emissions above the enhanced absorption regions (red) and other regions (black). Panel (c): Time profiles of average 10830 Å intensity over the enhanced absorption regions (red) and other regions (black). Panel (d): The correlation between EUV 131 Å emissions and 10830 Å intensity over the enhanced absorption regions.

observations are predominantly manifested in the high-precision measurement of the solar magnetic field. Consequently, following the realization of high-resolution narrowband imaging of 10830 Å, we intend to utilize NVST for research on near-infrared band polarization spectroscopy observation technology pertaining to the solar atmosphere. This endeavor aims to achieve high spatial, spectral, and temporal resolution along with high polarimetric sensitivity in spectropolarimetric measurements within the near-infrared band at NVST.

Acknowledgments

We acknowledge the insightful comments and suggestions provided by the referee. We extend our gratitude to the Kunming Institute of Physics for providing the infrared detector chips, a critical component that formed the basis of our observation. Special thanks are also due to the Nanjing Institute of Astronomical Optics and Technology for their contribution of the Lyot filter, enhancing the capabilities and precision of our observations. We are sincerely grateful to the

numerous individuals who offered their assistance, expertise, and encouragement throughout the course of this work. This work is supported by Yunnan Revitalization Talent Support Program (202305AS350029 and 202305AT350005) and Yunnan Key Laboratory of Solar Physics and Space Science (202205AG070009).

ORCID iDs

Wei-Jie Meng  <https://orcid.org/0009-0004-9119-6543>

References

- Avrett, E. H., Fontenla, J. M., & Loeser, R. 1994, in IAU Symp., 154, Infrared Solar Physics, ed. D. M. Rabin, J. T. Jefferies, & C. Lindsey (Dordrecht: Kluwer), 35
- Cao, W., Goode, P. R., Ahn, K., et al. 2012, in ASP Conf. Ser. Vol. 463, Second ATST-EAST Meeting: Magnetic Fields from the Photosphere to the Corona (San Francisco, CA: ASP), 291
- Chae, J., Park, H.-M., Ahn, K., et al. 2013, *SoPh*, 288, 1
- Harvey, J. W., & Livingston, W. C. 1994, in IAU Symp. 154, Infrared Solar Physics, ed. D. M. Rabin, J. T. Jefferies, & C. Lindsey (Dordrecht: Springer), 59
- Hashim, P., Xu, F., Wang, Y., et al. 2024, *ApJ*, 964, 157
- Hong, Z.-X., Yang, X., Wang, Y., et al. 2017, *RAA*, 17, 25
- Jaeggli, S. A., Lin, H., Onaka, P., et al. 2022, *SoPh*, 297, 137
- Ji, H., Cao, W., & Goode, P. R. 2012, *ApJL*, 750, L25
- Ji, K., Liu, H., Jin, Z., Shang, Z., & Qiang, Z. 2019, *ChSBU*, 64, 1738
- Lemen, J. R., Title, A. M., Akin, D. J., et al. 2012, *SoPh*, 275, 17
- Li, Q., Jin, L., & Li, G. 2021, *Chin. J. Liq. Cryst. Disp.*, 36, 327
- Liu, H., Jin, Z., Xiang, Y., & Ji, K. 2022, *RAA*, 22, 095005
- Liu, Z., Xu, J., Gu, B.-Z., et al. 2014, *RAA*, 14, 705
- Pesnell, W. D., Thompson, B. J., & Chamberlin, P. C. 2012, *SoPh*, 275, 3
- Regalado Olivares, S., López López, R., González, F., et al. 2022, *Proc. SPIE*, 12188, 121885B
- Scherrer, P. H., Schou, J., Bush, R. I., et al. 2012, *SoPh*, 275, 207
- Trujillo Bueno, J., Landi Degl'Innocenti, E., Collados, M., Merenda, L., & Manso Sainz, R. 2002, *Natur*, 415, 403
- Xu, Z., Jin, Z. Y., Xu, F. Y., & Liu, Z. 2014, in IAU Symp. 300, Nature of Prominences and Their Role in Space Weather, ed. B. Schmieder, J.-M. Malherbe, & S. T. Wu (Cambridge: Cambridge Univ. Press), 117